Physics of the Earth and Planetary Interiors 263 (2017) 23–37

Contents lists available at ScienceDirect

Physics of the Earth and Planetary Interiors

journal homepage: www.elsevier.com/locate/pepi

A discontinuous Galerkin method with a bound preserving limiter for the advection of non-diffusive fields in solid Earth geodynamics

Ying He [a,*], Elbridge Gerry Puckett [a], Magali I. Billen [b]

[a] Department of Mathematics, U. C. Davis, Davis, CA 95616, USA
[b] Department of Earth and Planetary Science, U. C. Davis, Davis, CA 95616, USA

ARTICLE INFO

Article history:
Received 22 May 2016
Received in revised form 22 November 2016
Accepted 8 December 2016
Available online 24 December 2016

Keywords:
Geodynamics
Composition advection
Discontinuous Galerkin method
Stokes equation
Bound preserving limiter
Strong stability preserving (SSP) Runge–Kutta

ABSTRACT

Mineral composition has a strong effect on the properties of rocks and is an essentially non-diffusive property in the context of large-scale mantle convection. Due to the non-diffusive nature and the origin of compositionally distinct regions in the Earth the boundaries between distinct regions can be nearly discontinuous. While there are different methods for tracking rock composition in numerical simulations of mantle convection, one must consider trade-offs between computational cost, accuracy or ease of implementation when choosing an appropriate method. Existing methods can be computationally expensive, cause over-/undershoots, smear sharp boundaries, or are not easily adapted to tracking multiple compositional fields. Here we present a Discontinuous Galerkin method with a bound preserving limiter (abbreviated as DG-BP) using a second order Runge–Kutta, strong stability-preserving time discretization method for the advection of non-diffusive fields. First, we show that the method is bound-preserving for a point-wise divergence free flow (e.g., a prescribed circular flow in a box). However, using standard adaptive mesh refinement (AMR) there is an over-shoot error (2%) because the cell average is not preserved during mesh coarsening. The effectiveness of the algorithm for convection-dominated flows is demonstrated using the falling box problem. We find that the DG-BP method maintains sharper compositional boundaries (3–5 elements) as compared to an artificial entropy-viscosity method (6–15 elements), although the over-/undershoot errors are similar. When used with AMR the DG-BP method results in fewer degrees of freedom due to smaller regions of mesh refinement in the neighborhood of the discontinuity. However, using Taylor–Hood elements and a uniform mesh there is an over-/undershoot error on the order of 0.0001%, but this error increases to 0.01–0.10% when using AMR. Therefore, for research problems in which a continuous field method is desired the DG-BP method can provide improved tracking of sharp compositional boundaries. For applications in which strict bound-preserving behavior is desired, use of an element that provides a divergence-free condition on the weak formulation (e.g., Raviart–Thomas) and an improved mesh coarsening scheme for the AMR are required.

1. Introduction

Study of the deformation and evolution of the solid Earth relies on computational geodynamics to explore a range of scientific questions from the origin of tectonic plates (Tackley, 2000) and large low seismic velocity provinces imaged in the lower mantle (Karason and van der Hilst, 2000; McNamara and Zhong, 2004), to the processes governing subduction dynamics (Gurnis and Hager, 1988; Christensen, 1996), spreading at mid-ocean ridges (Gerya, 2010), and long term mixing of geochemical signatures in the deep mantle (Christensen, 1989; Kellogg, 1991; Kellogg et al., 1999). Because compositionally-distinct regions exist within both tectonic plates and the mantle, the importance of modeling the complete thermo-chemical evolution of these systems has long been recognized and incorporated into computational studies (e.g., Davies, 1977; Hoffman and McKenzie, 1985). However, modeling the time evolution of compositional fields is challenging because these fields are non-diffusive, and thus require methods that can track sharp boundaries. In addition, while there are finite element methods that are well suited for solving the advection–diffusion equation for the diffusive temperature field, these same methods can be unstable or lead to unwanted smearing of boundaries when applied to a non-diffusive variable (Zhong et al., 2007).

Several approaches employed by the solid Earth geodynamics community to address the computational challenges of advecting

* Corresponding author.
E-mail address: yinghe@math.ucdavis.edu (Y. He).

http://dx.doi.org/10.1016/j.pepi.2016.12.001
0031-9201/

a non-diffusive compositional field include (Zhong et al., 2007): (1) a small, but non-zero artificial diffusivity used to stabilize the standard methods (Kellogg, 1991; Kellogg and King, 1993), (2) a non-linear shock capture technique used to remove over/undershoots and sharpen the compositional boundary (Lenardic and Kaula, 1993), and (3) tracer particles used instead of a continuous field (Christensen, 1989; Tackley and King, 2003; Gerya and Yuen, 2003a; McNamara and Zhong, 2004; Moresi et al., 2003). Each of these approaches has benefits and costs, most notably that field-based methods (i.e., a continuous variable similar to temperature) tend to smooth sharp boundaries, while active tracer methods require additional software infrastructure to implement and can be more expensive computationally. Before describing these methods and considering their strengths and weaknesses, it is useful first to consider two examples of how compositionally distinct regions enter into geodynamic simulations.

1.1. Non-diffusive fields in the geodynamical simulations

Two examples of geodynamic processes are illustrated in Fig. 1: subduction of a tectonic plate and upwelling of a compositional *pile* at the base of the mantle. In both cases there are compositionally distinct regions (i.e., layers, blobs) and the properties of these materials (e.g., density, viscosity, radiogenic heating) may depend on the composition. Therefore, any approximations or errors in the advection of the compositional field will contribute to approximations or errors in the solution of the Stokes and the thermal advection–diffusion equations.

Subduction Zone In the case of subduction, the main compositional structure is that of layering within the tectonic plates including sediments, crust, a residuum left-over after melting and the mantle (Fig. 1a). The subducting plate forms at a spreading center due to melting of the mantle with an approximately pyrolitic composition. Melting creates a thin crustal layer (5–10 km) overlying a residuum layer (15–25 km thick) composed of primarily olivine (e.g., harzburgite composition; Oxburgh and Parmentier (1977)). The boundary between the crust and residuum layer is sharp (a few hundred meters), while the boundary between the residuum and the pyrolitic mantle is gradational over tens of kilometers (Fischer et al., 2010). Similarly, the continental or overriding plate has a thicker crust (30–70 km) and residuum layer (up to ≈150 km), and the composition of these layers differ from each other and from these same layers in the oceanic plate.

While the mantle below tectonic plates does have heterogeneities in composition or geochemical signatures, these are not usually of primary interest for these types of subduction studies and therefore this layer is treated as compositionally homogeneous. One exception is the tracking of composition related to movement of volatile components, which can cause changes in the mineralogy and melting within the mantle wedge (Gerya and Yuen, 2003b). For this system, tracking of composition includes tracking all the layers within the tectonic plates, as well as the entrainment and mixing of material into the mantle wedge above the subducting plate.

Compositional Piles Large regions with low seismic velocity in the lower mantle have been interpreted as irregular layers of compositionally distinct material (e.g., Kellogg et al., 1999; Zhao et al., 2015). Simulations involving this kind of compositionally-distinct region often include modeling the evolution of the whole mantle over the age of the Earth. In these simulations the focus is on how piles are moved around and deformed through interaction with the large-scale mantle flow as well as entrainment of parts of this layer into rising thermal plumes that form on or near the piles (Kellogg et al., 1999; McNamara and Zhong, 2005; Lin and van Keken, 2005; Tackley, 2012). Entrainment of this material into hot rising plumes is inferred from the geochemical signatures measured in rocks erupted at the Earth's surface (e.g., Hofmann, 1997). Seismic observations suggest that the boundaries of these piles are sharp in some regions (e.g., Garnero and McNamara, 2008). In addition the possible preservation of these regions over >4.0 billion years suggest that sharp boundaries are maintained by distinct material properties.

1.2. Previous methods for tracking non-diffusive fields

The examples described above illustrate that for a range of geodynamical studies it is necessary to accurately track large continuous regions with sharp boundaries, as well as, properly treat the entrainment and mixing of these components over long timescales. In the geodynamics literature two approaches have been used to track compositional variations within mantle convection simulations: field methods and tracer methods. Field methods commonly implement the Stream-line Upwind Petrov–Galerkin method (SUPG; Brooks and Hughes (1982)), which is also commonly used to solve the energy equation (e.g., ConMAN, King et al., 1990; Citcom, Moresi and Solomatov (1995), Zhong et al. (2000)). However, for non-diffusive fields, the SUPG method will lead to overshoots/undershoots of the composition. In early models, overshoots/undershoots were addressed by adding a small artificial diffusivity characterized by the Lewis number (Le $= 1/\kappa$,

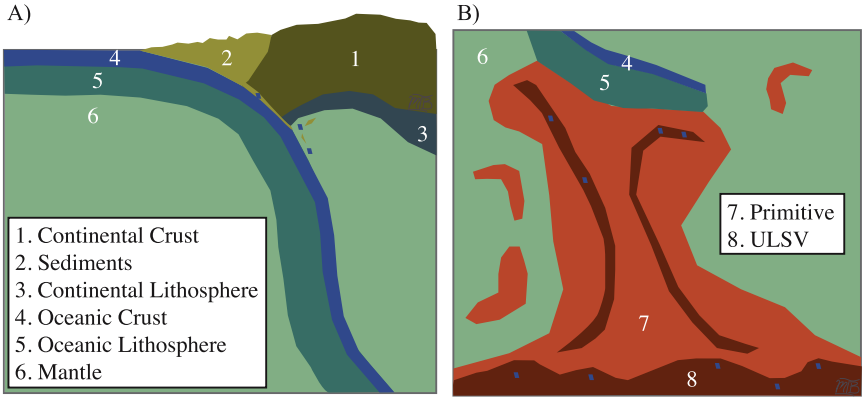

Fig. 1. Illustration of compositional variability in (A) an upper mantle subduction zone, and (B) the lower mantle near a compositional pile. Compositional variability exists as layers with both sharp (crust/lithosphere) and gradational (lithosphere/mantle) boundaries within the tectonic plates and at the base of the mantle, but these layers are stretched, broken, mixed and entrained by mantle flow. Multiple distinct compositional types need to be accurately tracked throughout this process. (For interpretation of the references to colour in this figure legend, the reader is referred to the web version of this article.)

where κ is the diffusivity; Kellogg (1991); Kellogg and King (1993); Christensen (1989)). The use of a compositional field (rather than tracers) has the advantage of using the same solver method as that used for the thermal field and, depending on details of the implementation, using less memory to attain the same level of accuracy. For these early models, resolution was severely limited by computational resources, so this approximation was reasonable. However, as computational power increased and understanding related to compositional structures in the mantle improved, so too has the need for more accurate modeling of truly non-diffusive fields.

One of the first improvements was to adapt a two-step, nonlinear shock capture method to mantle convection problems (Lenardic and Kaula, 1993). This method removes dispersion errors by applying a global filter to remove any values that are above or below the defined minimum and maximum of the field. This method has been applied within several computational codes using advection of compositional fields (e.g., Farnetani and Richards (1995); Moresi and Lenardic (1997); Tackley and King (2003)). More recently Kronbichler et al. (2012) implemented the entropy-viscosity (ν_k) stabilization scheme originally proposed in Guermond et al. (2011) to obtain correct solutions to problems with high Péclet number, such as mantle convection. In these problems, the standard finite element discretizations introduce spurious oscillations around steep gradients (Donea and Huerta, 2005). The entropy-viscosity stabilization removes such oscillations, but tends to smooth and broaden initially sharp boundaries.

The use of tracer particles to track compositional fields in geodynamical simulations began with applying the marker chain method to track the boundary between two compositions (e.g., Woidt, 1978; Christensen, 1982). In two dimensional (2-D) simulations, this results in a chain of roughly evenly-spaced particles, and is a cost effective tracer method as it uses few tracers to track only the boundary at high resolution. However, the number of tracers can quickly increase for models with fine grids, or with mixing of the material, which can lead to exponential growth in the length of the boundary (van Keken et al., 1997). It is also difficult to extend the marker chain method to three dimensional (3-D) models.

More recently, the level set method has been applied in geodynamical problems to track the interface between two compositions (Suckale et al., 2010; Samuel and Evonuk, 2010). Unlike the marker-chain method, which tracks the boundary between two compositions, the level-set method tracks a surface whose zero contour is the boundary between the two compositions. Level set methods have the advantage of working well in both 2-D and 3-D, and easily tracking surfaces that fold and break apart. One challenge in implementing level-set method is tracking multiple (> 2) compositional fields.

More general tracer methods have become a popular approach for including multiple compositional fields into geodynamical solutions, and offer the unique advantage of being able to track the history of strain of a volume of material, which can be related to observable seismic properties (e.g., seismic anisotropy). Tracer particles have been added to existing eulerian, finite element method (FEM) and finite difference (FD) simulation codes (McNamara and Zhong, 2004; Tackley and King, 2003; Gerya and Yuen, 2003a) or more explicitly included through Lagrangian particle-in-cell (PIC) methods, in which the tracers become the integration points within an element on the Eulerian grid (O'Neill et al., 2006).

One advantage of using tracers rather than a field is that there is no explicit diffusion or dispersion at the boundary between two compositional fields. Instead, the solution to the incompressible Stokes equations is applied to advect the tracers, and then the tracer properties are used to update the material properties for the next time step. However, this last step can effectively lead to smoothing of sharp boundaries due to interpolation from the tracers to the grid. Lagrangian PIC methods avoid this smoothing by making the tracers the integration points. The main limitations of tracers are the increased computational overhead and need to support an additional computational scheme.

1.3. Discontinuous Galerkin (DG) method with a bound preserving limiter

To improve the solution for the advection of non-diffusive fields in geodynamics applications, we look to other disciplines for possible methods. The aim is to find a stable, efficient approach to accurately advect compositional fields while preserving the sharp discountinuities that exist in these problems. One such approach is the Discontinous Galerkin method, which by-passes the continuous shape functions used to represent quantities in the FEM to allow for discontinuities. Here, we present a new method of addressing the stability of the non-diffusive field advection problem in geodynamics simulations. Specifically, we apply a Discontinuous Galerkin (DG) method (Cockburn and Shu, 1998), which stabilizes the advection equation by a monotone upwind flux and a bound preserving (BP) limiter (Zhang and Shu, 2010b; Zhang et al., 2013).

The DG method was first introduced to solve the hyperbolic neutron transport equation (Reed and Hill, 1973). Later, Runge–Kutta Discontinuous Galerkin (RKDG) methods were developed for hyperbolic conservation laws (Cockburn and Shu, 1989; Cockburn et al., 1990; Cockburn and Shu, 1998). More recently, a uniformly high order accurate DG scheme, which preserves positivity of density and pressure for the compressible Euler equations of the gas dynamics was constructed (Zhang and Shu, 2010b). Subsequently, a second order accurate DG scheme was designed, which satisfies a strict maximum principle for general nonlinear convection diffusion equations on unstructured triangular meshes (Zhang et al., 2013).

The potential for the DG method to be a good alternative approach to solving the energy equation for mantle convection was first suggested (but not implemented) by Burstedde et al. (2013). The DG method has also recently been applied to simulations of mantle convection using the FEniCS framework to study the time-dependent isothermal compositional convection (Rayleigh–Taylor instability) benchmark problem (Vynnytska et al., 2013). In that study, the incompressible Stokes equations are discretized using standard finite element method with Taylor–Hood elements (Taylor and Hood, 1973). The discretization of the compositional equation is carried out by an implicit Euler scheme in time, the DG method in space, and a shock capture filtering method is used to correct for numerical dispersion (Lenardic and Kaula, 1993). Their numerical examples demonstrate that the discontinuous Galerkin scheme is an effective alternative for tracking compositional interfaces without significant numerical diffusion or dispersion errors. However, as can be seen in the figures presented on that study, the shock-capture filtering method does not preserve any bound property and significant errors in the compositional field still exist near the boundaries.

1.4. Overview of work presented

We first present the DG method with a bound preserving limiter (BP limiter) to solve the compositional equation for a given static circular flow centered in a square box. Then we apply the same approach to the falling box problem, and compare our numerical results with a FEM approach using entropy viscosity stabilization. The aim of the work presented here is not only tracking compositional interfaces without significant numerical diffusion or disper-

sion errors, but also to preserve the global bound of the composition. The global bound on the composition is an important physical property, as any overshoot or undershoot of the composition will be strongly amplified by the compositionally-dependent viscosity or density and will therefore directly impact the solution to the Stokes problem.

To the best of our knowledge, there is no related work on DG, RKDG or Local Discontinuous Galerkin (LDG) methods applied to solid Earth geodynamics modeling problems with the BP limiter, and in particular as to the equations of mantle convection. Therefore, we present the computational scheme required for applying of the DG method with BP limiter within a FEM mantle convection simulation code. Specifically, we first describe the governing equations for our model problem and formulate its weak form after we use the IMPES (implicit pressure explicit saturation) approach to solve the nonlinear problem between the incompressible Stokes equations and compositional equation (Section 2.1). Next, we briefly discuss the spatial discretization by the FEM for the Stokes Problem (Section 2.2). Then, we present the FEM and the DG discretization for the composition problem (Sections 2.3 and 2.4), and the BP limiter used to stabilize the DG scheme (Section 2.5). Finally, we review the Adaptive mesh refinement (AMR) technique used in the work (Section 2.6).

To verify our numerical schemes and to demonstrate their efficiency and stability we present some numerical results using a problem called the falling box (Gerya and Yuen, 2003a) described in Section 3.2. We chose the falling box problem because we require a test problem that reproduces the dynamic conditions under which other advection schemes commonly fail – that is, strongly advection-dominated flow within a mantle convection simulation. Second, we require a problem that provides physical structures that will test our ability to capture and resolve the deforming compositional boundary interface. A box, with sharp corners (rather than a sphere) provides a quite challenging test case, in particular (as will be shown), with the development of long, thin tails from the top two corners in the isoviscous case. We compare the results and performance of the DG-BP method with a FEM using a viscosity-entropy scheme (Section 3.4) for solving the compositional advection equation. We find that the DG method with a BP limiter provides stable solutions with sharper compositional boundaries and is computationally more efficient (i.e., fewer degrees of freedom). We also show that choice of time integration scheme is key to obtaining non-oscillatory results with the BP limiter.

2. Methods

The model problem we consider is described by the equations of conservation of linear momentum and mass – the incompressible Stokes equations, and the advection of a non-diffusive quantity, C:

$$
\begin{aligned}
&-\nabla\cdot(2\eta(C)\epsilon(\mathbf{u}))+\nabla p=\rho(C)\mathbf{g},\\
&\nabla\cdot\mathbf{u}=0,\\
&\frac{\partial C}{\partial t}+\mathbf{u}\cdot\nabla C=0,
\end{aligned}
$$

where $\mathbf{u}$ is the velocity, p is the pressure, C is the composition, $\epsilon(\mathbf{u})=\frac{1}{2}(\nabla\mathbf{u}+(\nabla\mathbf{u})^{\mathbf{T}})$ is the strain-rate tensor, $\rho(C)=\rho_0+(\rho_1-\rho_0)C$ is the composition-dependent density, and $\eta(C)=(\frac{\eta_1}{\eta_0})^{C}\eta_0$ the composition-dependent viscosity with positive constant reference densities ($\rho_0\leqslant\rho_1$) and viscosities ($\eta_0\leqslant\eta_1$). These equations are solved with no-flux boundary conditions: $\mathbf{u}\cdot\mathbf{n}=0$.

One should notice that Eqs. (1b), (1c) imply

$$\frac{\partial C}{\partial t}+\nabla\cdot(\mathbf{u}C)=0. \tag{2}$$

which is the conservative form of the equation for advection of the compositional field C and is the preferred form to use with the DG method.

2.1. Nonlinear decoupling and time discretization

The incompressible Stokes equations can be considered as a constraint on the compositional equation at any given time. It makes the system highly nonlinear. To solve this nonlinear system, we apply the IMPES approach to decouple the incompressible Stokes equations and compositional equation, which leads to two linear equations (the Stokes equations and the compositional equation) and they can be solved easily and efficiently. Specifically, given the initial time t_0, time-step size $\triangle t$ and the initial composition field C^0, at current time $t_k=t_0+k\cdot\triangle t$, we solve for current velocity $\mathbf{u}^k$ and pressure p^k from the incompressible Stokes Eqs. (3a), (3b) using the composition field C^k from the current time-step $k=0,1,\cdots$, as shown below

$$-\nabla\cdot(2\eta(C^k)\epsilon(\mathbf{u}^k))+\nabla p^k=\rho(C^k)\mathbf{g}, \tag{3a}$$

$$\nabla\cdot\mathbf{u}^k=0. \tag{3b}$$

Then we solve the next time step composition filed C^{k+1} but, with the velocity field from the previous time steps. The choice of time discretization scheme depends on the method used for the spatial discretization. For the case when the FEM is used for the spatial discretization, we use the same semi-implicit BDF2 scheme as shown in Kronbichler et al. (2012) except we fix the time-step size $\triangle t$ for simplicity. However, if the DG method is used, then a Strong Stability-Preserving (**SSP**) high order time discretization method (Gottlieb, 2005; Gottlieb et al., 2001) is applied in order to maintain the bound preserving property from the limiter.

If the forward Euler method is stable under the time constriction $\triangle t<L$, then the SSP high order time discretization method satisfies the same stability under the time step restriction with a constant coefficient c given by $\triangle t<cL$. A simple optimal second order two stage **SSP** Runge–Kutta (RK) method with a constant $c=1$ is given by:

$$C^{k+1/2}=C^k+\triangle t\nabla\cdot(-\mathbf{u}^kC^k), \tag{4a}$$

$$C^{k+1}=\frac{1}{2}C^k+\frac{1}{2}C^{k+1/2}+\frac{1}{2}\triangle t\nabla\cdot(-\mathbf{u}^{k+\frac{1}{2}*}C^{k+1/2}), \tag{4b}$$

where $\mathbf{u}^{k+\frac{1}{2}*}$ can be obtained either by solving Eqs. (3a) and (3b) with $C^{k+1/2}$ or extrapolation by using numerical solutions at previous time steps.

Alternatively, one can use the second order SSP three-step method with a constant $c=\frac{1}{2}$ given by:

$$C^{k+1}=\frac{3}{4}C^k+\frac{3}{2}\triangle t\nabla\cdot(-\mathbf{u}^kC^k)+\frac{1}{4}C^{k-2}. \tag{5}$$

One should be aware that the given second order SSP three-step method (5) assumes that the time step size is a constant in time. However, the second order two stage **SSP** Runge–Kutta (RK) method (4a) and (4b) can still be applicable for variable time step size. We will show results for the DG method using both the RK and three-step time discretization schemes.

2.2. Spatial discretization for the Stokes problem

For the spatial discretization, the FEM is the only method applied for Eqs. (3a) and (3b), where we need to solve a discrete saddle point Stokes problem. For the composition advection prob-

lem both the FEM and DG method are applied separately with the FEM Stokes solver in order to compare their performance. Because the one focus of this paper is the comparison between the FEM and DG-BP method for solving the compositional advection equation, for the spatial discretization of the incompressible Stokes Eqs. (3a) and (3b) we used the same FEM approach as discussed in Kronbichler et al. (2012). Therefore, we refer the interested reader to Kronbichler et al. (2012) for a more detailed discussion of the spatial discretization and the choices of Stokes preconditioner.

2.3. FEM stabilization of the composition advection problem

For the purposes of testing and comparing the DG method developed here we also compute solutions using an FEM with entropy-viscosity stabilization (Kronbichler et al., 2012) for the composition advection equation. In this case the resulting matrix system is

$$MC^{k+1} = \frac{1}{3}M(4C^k - C^{k-1}) + \frac{2}{3}\triangle t \cdot G^k \tag{6}$$

where $\{\psi_j\}$ are the set of basis functions of the finite element space, M is the mass matrix with entries $(M)_{ij} = (\psi_j, \psi_i)_\Omega$, and the inner product $(\ ,\ )_\Omega$ for any two given functions ψ and ϕ is defined as below

$$(\psi, \phi)_\Omega = \int_\Omega \psi(x)\phi(x)dx. \tag{7}$$

The right hand side vector G^k is calculated using two previous time-step solutions C^k, C^{k-1} and $\mathbf{u}^k$, $\mathbf{u}^{k-1}$ by the formula

$$G_j^k = -(\mathbf{u}^{*,k}\nabla C^{*,k}, \psi_j)_\Omega - (v_h^k \nabla C^{*,k}, \nabla\psi_j)_\Omega \tag{8}$$

where v_h^k is the entropy viscosity function defined in Kronbichler et al. (2012). The entropy-viscosity function is constant within a cell, and only adds artificial diffusion where the local Péclet number is large and the solution is non-smooth. The extrapolated values for velocity and composition are defined as

$$\mathbf{u}^{*,k} = 2\mathbf{u}^k - \mathbf{u}^{k-1} \text{ and } C^{*,k} = 2C^k - C^{k-1}. \tag{9}$$

2.4. DG discretization of the composition advection problem

For the DG method the spatial discretization is different from the FEM because it must allow for discontinuities between elements. We first consider the theoretical basis for this method and then explain how it is implemented.

We denote our computational domain as $\Omega = \cup_{e=1}^{E}\Omega^e$, where Ω^e represents non-overlapping body-conforming quadrilateral elements. We consider a local approximate solution $u^e(x,y)$ that has the local nodal representation

$$u^e(x,y) = \sum_{i,j=0}^{N} u_{ij}^e \psi_{ij}^e(\xi(x), \eta(y)), \tag{10}$$

where $\{(x_i, y_j)\}_{i,j=0}^N$ denotes the set of grid points on Ω^e. The basis coefficients u_{ij}^e are the nodal values $u^e(x_i, y_j)$ on Ω^e, and the basis $\psi_{ij}(\xi,\eta) = \ell_i(\xi)\ell_j(\eta)$, or simply ψ_{ij}, has a tensor product form of multi-dimensional Nth-order Lagrange interpolation polynomials based on $N+1$ grid points in each direction. Grid points can be equidistant (FEM), or Gauss–Legendre-Lobatto (GLL) quadrature grid points (i.e., the Spectral Element Method).

We map each physical coordinate $(x,y) \in \Omega^e$ onto the reference domain $(\xi,\eta) \in I = [-1,1]^2$ through the affine mapping and formulate the computational scheme on the reference domain. Let us define a finite-dimensional approximation space $V_N \subset H^1(\Omega)$ such that $V_N = \text{span}\{\psi_{ij}^e(\xi,\eta)\}_{i=0,j=0,e=1}^{N,N,E}$. With this approximation space, one can represent the global solution as the direct sum of local piecewise polynomials

$$u(x,y) \simeq u_h(x,y) = \bigoplus_{e=1}^{E} u_h^e(x,y), \tag{11}$$

where $u_h^e(x,y)$ is defined on each element Ω_e by Eq. (10). At the overlapping interfaces the DG space functions do not require any continuity, which is the main difference compared with the continuous Galerkin approach.

When the DG method is applied after the spatial discretization of Eq. (4a) and (4b), for the weak formulation one must find $C^{k+1} \in V_N$ such that

$$(C^{k+1/2}, w)_{\Omega_e} = (C^k, w)_{\Omega_e} + \triangle t(C^k\mathbf{u}^k, \nabla w)_{\Omega_e} - \triangle t(\mathbf{u}^k \cdot \mathbf{n}C^{k,*}, w)_{\partial\Omega_e}, \tag{12}$$

$$(C^{k+1}, s)_{\Omega_e} = \frac{1}{2}(C^k + C^{k+\frac{1}{2}}, s)_{\Omega_e} + \frac{1}{2}\triangle t(C^{k+\frac{1}{2}}\mathbf{u}^{k+\frac{1}{2}}, \nabla s)_{\Omega_e} - \frac{1}{2}\triangle t(\mathbf{u}^{k+\frac{1}{2},*}C^{k+\frac{1}{2}}, s)_{\partial\Omega_e}, \tag{13}$$

for any $w, s \in V_N$. An upwind flux is used for $C^{j,*}$ where $j = k, k+1/2$ (Cockburn and Shu, 1998; Hesthaven et al., 2008) and is defined as

$$C^{j,*} = \begin{cases} C^{j,-}, & \text{if } \mathbf{u}^j \cdot \mathbf{n} > 0 \\ C^{j,+}, & \text{if } \mathbf{u}^j \cdot \mathbf{n} < 0 \end{cases} \tag{14}$$

where $C^{j,-}$ is the local/interior solution on Ω_e, and $C^{j,+}$ is the neighbor/exterior solution of Ω_e. Although, Eqs. (12) and (13) appears to be only defined locally on each element Ω_e, it actually also depends on the adjacent solutions through the flux term $C^{j,*}$, which is defined at each element interface using two side values. Generally, the flux term $C^{j,*}$ is the most difficult part to determine when one wants to design a DG scheme, as it is the key point used to ensure the scheme's stability.

If we consider the following DG numerical expansions in V_N

$$C^{\hat{k}_1}(x,y) = \bigoplus_{e=1}^{E}\sum_{i,j=0}^{N} C_{ij}^{\hat{k}_1,e}\psi_{ij}^e(\xi(x),\eta(y)),\ \hat{k}_1 = k+1, k+1/2, k \tag{15}$$

$$\mathbf{u}^{\hat{k}_2}(x,y) = \bigoplus_{e=1}^{E}\sum_{i,j=0}^{N} \mathbf{u}_{ij}^{\hat{k}_2,e}\psi_{ij}^e(\xi(x),\eta(y)),\ \hat{k}_2 = k+1/2, k \tag{16}$$

and the mass matrix $\bar{M} = diag(M^1, \cdots, M^E)$ where

$$(M^e)_{\bar{i}\bar{j},ij} = (\psi_{ij}^e(\xi(x),\eta(y)), \psi_{\bar{i}\bar{j}}^e(\xi(x),\eta(y)))_{\Omega e}\ e = 1, \cdots, E, \tag{17}$$

the inner product $(\ ,\ )_{\Omega_e}$ for any two given functions ψ and ϕ on a cell Ω_e is defined as below

$$(\psi, \phi)_{\Omega_e} = \int_{\Omega_e} \psi(x)\phi(x)dx. \tag{18}$$

and the right hand side vector $\overline{G}^{\hat{k},*} = (G^{\hat{k},1}, \cdots, G^{\hat{k},E})^T$, $\hat{k} = k, k+1/2$, where

$$(G^{\hat{k},e})_{\bar{i}\bar{j}} = (C^{\hat{k}}\mathbf{u}^{\hat{\mathbf{k}}}, \nabla\psi_{\bar{i}\bar{j}}^e(\xi(x),\eta(y)))_{\Omega_e} - (\mathbf{u}^{\hat{\mathbf{k}}} \cdot \mathbf{n}C^{\hat{k},*}, \psi_{\bar{i}\bar{j}}^e(\xi(x),\eta(y)))_{\partial\Omega_e} \tag{19}$$

then the matrix system of equation is given by

$$\overline{M}C^{k+1/2} = \overline{M}C^k + \triangle t \cdot \overline{G}^{k,*}, \tag{20}$$

$$\overline{M}C^{k+1} = \frac{1}{2}\overline{M}C^k + \frac{1}{2}\overline{M}C^{k+1/2} + \frac{1}{2}\triangle t \cdot \overline{G}^{k+1/2,*}. \tag{21}$$

2.5. Adding a Bound-Preserving (BP) Limiter

Following an idea similar to that presented by Zhang and Shu (2010b), after each time-step a BP limiter is applied to the newly obtained numerical solution C^{k+1} in a post-processing procedure. Therefore, we modify the scheme in Eqs. (20) and (21)as follows

$$\overline{M}C^{k+1/2} = \overline{M}\tilde{C}^{k} + \triangle t \cdot \overline{G}^{k,*}, \tag{22a}$$

$$\tilde{C}^{k+1/2} = \mathrm{BPLimiter}(C^{k+1/2}), \tag{22b}$$

$$\overline{M}C^{k+1} = \frac{1}{2}\overline{M}\tilde{C}^{k} + \frac{1}{2}\overline{M}\tilde{C}^{k+1/2} + \frac{1}{2}\triangle t \cdot \overline{G}^{k+1/2,*}, \tag{22c}$$

$$\tilde{C}^{k+1} = \mathrm{BPLimiter}(C^{k+1}) \tag{22d}$$

where BPLimiter$(\cdot)$ represents the BP limiter applied to the DG solution of (22a) or (22c). At time step k, if the DG solution is bounded by $C_m \leqslant C^k \leqslant C_M$, then after applying the limiter, the solution $\tilde{C}^{k+1}$ is guaranteed to satisfy the same upper and lower bounds $C_m \leqslant \tilde{C}^{k+1} \leqslant C_M$.

In previous studies three key ingredients required for constructing a high order maximum-principle-satisfying DG scheme were introduced (Zhang and Shu, 2010b; Zhang et al., 2013):

1. The composition cell average at the next time step by forward Euler time discretization scheme is a monotone function with respect to certain point values (Gauss–Lobatto points for the one-dimensional case), under a suitable CFL condition.
2. A simple scaling limiter modifies the DG polynomial $p(x)$ on cell I_e into $\tilde{p}(x)$ such that $\tilde{p}(x) \in [C_m, C_M]$ at these special points without changing its cell average. Moreover, it can be proven that the modified polynomial $\tilde{p}(x)$ is also a high order approximation just as $p(x)$. Thus we have $\bar{C}^{k+1} \in [C_m, C_M]$ if all the degrees of freedom at time level k in the right hand side of Eq. (20) are replaced by using those of modified polynomials $\tilde{p}(x)$.
3. The forward Euler method is replaced by a strong stability preserving (SSP) high order time discretization scheme, which is a convex combination of forward Euler and thus, will preserve the bounds.

In our work, we follow these steps to post-process the numerical solution $C^{k+j}, j = 1/2, 1$ in (22a/22c) in order to obtain a modified solution $\tilde{C}^{k+j}$ such that its DG polynomials at certain special points (see Zhang and Shu (2010a)) are bound preserved and] the cell average satisfies

$$\tilde{\bar{C}}^{k+j} = \bar{C}^{k+j} \in [C_m, C_M], j = 1/2, 1, \tag{23}$$

which is then used again in the next time step to ensure the cell average $\bar{C}^{k+2}$ is also bound preserved.

In addition, in Zhang and Shu (2010a) Section 4 "Application to Two dimensional Incompressible Flows", the authors discuss how to take advantage of maximum-principle-satisfying high order schemes for scalar conservation laws to construct schemes for passive convection equations with a divergence free velocity field. In particular, they prove that a point-wise divergence free velocity field is a sufficient condition for the limiter to strictly preserve the bound: i.e. Eq. (23). In this work, we also studied our DG-BP method with and without a divergence free velocity field. This will be discussed in the section on numerical results.

2.6. Adaptive mesh refinement

Adaptive Mesh Refinement (AMR) is an algorithm for refining or coarsening the grid subject to a user defined criteria such as the temperature or strain-rate gradient across a cell (Berger and Oliger, 1984; Verfürth, 1996). AMR has been broadly applied in the area of scientific computing and, in particular, in the field of computational geodynamics and mantle convection (Kronbichler et al., 2012), since generally the goal is to make well-refined 3D computations. The advantage of AMR is that it provides the same overall accuracy as a uniformly refined grid with the same, given minimum grid size, but the numerical cost is significantly reduced by coarsening the grid in regions where a less refined grid is sufficiently accurate. In our numerical computations in which we use AMR, we use the Kelly error indicator (Kelly et al., 1983) applied to the compositional field to determine when to refine or coarsen the mesh.

Given a polynomial basis of a fixed degree the accuracy of the DG and FEM methods is primarily determined by the overall minimum grid size. However, with a uniformly refined grid, the total degrees of freedom for the DG method is greater than that for the FEM, since the DG method requires extra degrees of freedom at the element boundaries. On the other hand, if we use AMR, it is no longer necessarily true that the DG method requires more degrees of freedom than FEM, since a greater number of FEM elements are typically required to resolve the compositional boundary, which is smeared out over more elements. Indeed, our numerical results show that for problems with a discontinuity, with AMR the cost of in terms of the total number of degrees of freedom for the DG method is less than that for FEM.

3. Numerical results

3.1. Advection in a 2D circular flow

In our first computation we study the movement of a 0.25×0.25 square in a two dimensional steady flow, $\mathbf{u} = (-y, x)$, defining a circular flow about the center of a box. This flow is an exact solution of the incompressible Stokes equations and is therefore *pointwise* divergence-free. Initially the center of the box is placed at the point $(0.5, 0)$ inside a square domain with dimensions of $[-1, 1] \times [-1, 1]$ as shown in Fig. 2 (A). In this computation, since the velocity field is known, we are only computing the solution of advection equation for the composition field. We ran this computation using a second order DG element and a time-step size of $\triangle t = 0.00025$ for three different meshes:

B) A uniform mesh with 256×256 cells;
C) An AMR mesh with a minimum global mesh size of $h = 1/128$, allowing coarsening and refinement of the mesh;
D) An AMR mesh with a minimum global mesh size of $h = 1/128$, but only allowing refinement of the mesh (no coarsening).

The results of this computation after the compositionally-defined square has returned to its initial position at $t = 6.283 \approx 2\pi$ are displayed in Fig. 2(B)–(D) and quantitatively summarized in Table 1. Note that in all three computations the amount of overshoot and undershoot is $O(10^{-10})$ for the final time, which is well within the expected accuracy of the numerical solution of the advection equation.

The maximum value of the composition for three different grids with $h = 1/128$ are displayed as a function of the model time in Fig. 3. On a uniform mesh, we find that there is no over-/undershoot (Fig. 3(B)). This example confirms that for the case of a divergence-free flow, the DG-BP method is indeed bound-preserving. For the case using AMR with both refinement and coarsening, overshoot occurs at the start of the computation, and then decreases with time (Fig. 3(A)). The maximum composition spikes again as the direction of the motion changes at every $\pi/2$ rotation of the square ($t = (0, \pi/2, \pi, 3\pi/2)$). In order to determine

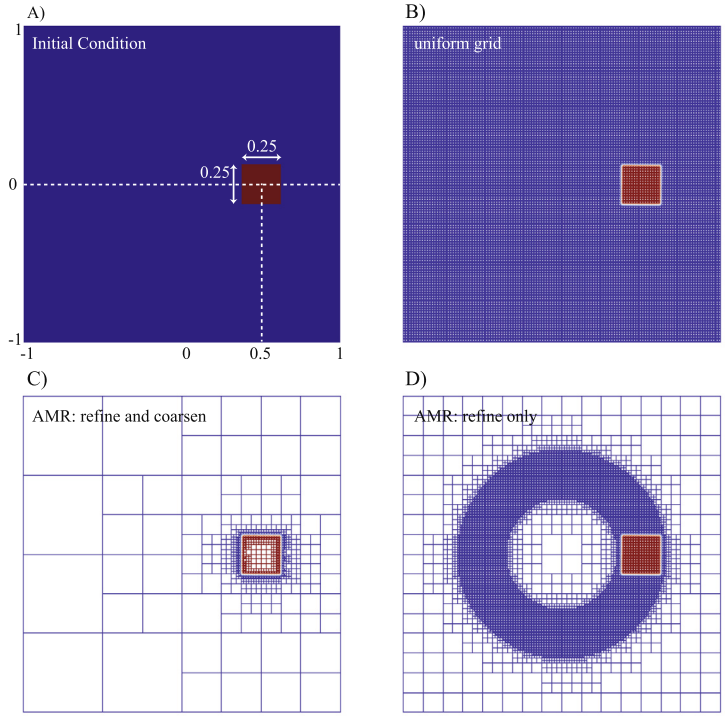

Fig. 2. A 2D Circular Flow. (A) Initial position of the compositionally-defined red square. (B) The numerical result after a rotation of 2π on a uniform mesh with 256×256 cells. (C) The numerical result after a rotation of 2π on an AMR mesh allowing both coarsening and refinement of the mesh (with a minimum global mesh size of $h = 1/128$). (D) The numerical result after a rotation of 2π on an AMR mesh only allowing refinement of the mesh (minimum global mesh size of $h = 1/128$). All three computational results are shown at the final time $t = 6.283 \approx 2\pi$.

Table 1
2D Circular Flow Results. Values listed are after one rotation of the square; i.e., at $t = 6.283 \approx 2\pi$. All computations have a minimum grid size of $h = 1/128$. For the case with refinement only, the overshoot only occurs at times from $t = 0.0335$ to 0.03725.

	Final Time $t = 6.283 \approx 2\pi$				All Times	
Grid	# Cells	# DOFs (C)	Max(C)	Min(C)	Max(C)	Time
Uniform Mesh	65536	589824	1.0	−9.85052e−11	1.0	
AMR (refine and coarsen)	1192	10728	$1 + O(10^{-11})$	−8.07723e−11	1.022	$t = 0.0245$
AMR (refinement only)	17554	157,986	$1 + O(10^{-11})$	−9.46702e−11	1.00038	$t = 0.03475$

the source of this error, we ran a third case in which we allow only refinement of the mesh (Fig. 3(C)). In this case, there is a small spike in the maximum of composition value near the start of the computation, but afterwards the maximum value remains at 1.0. These two computations demonstrate that there is an error introduced in the AMR coarsening algorithm. This error occurs because the cell average of the composition field is not preserved during the coarsening operation. It is likely this algorithm can be modified so that the cell average of the composition field is conserved. However, this is a part of the deal.II library and will require the cooperation of the individuals who maintain it http://dealii.org/. While the computation on the uniform mesh produces no overshoot or undershoot, it does require significantly more grid cells and thus more degrees of freedom than either of the two computations with AMR (Table 1).

To quantify the sharpness of the compositional boundary, we measure the jump of the interface along the x-axis near the point $(0.375, 0)$ at the final time $t = 6.283$. First, we find that all three different grids produce nearly identical profiles along the x-axis. The jump at the composition interface near the point $x = 0.375$ occurs between the points $x = 0.356$ and $x = 0.392$, and the corresponding composition values are 0.00338162 and 0.994706, which is within three digits of accuracy (less than the mesh width h) of the target values of 0.0 and 1.0. The distance between the two points is $0.036 \approx 4.608h$, which is less than the width of five cells with $h = 1/128$. Next, we re-ran all three tests with a *larger* mesh size $h = 1/64$. At the final time $t = 6.283$ with a second order DG element and time-step size $\triangle t = 0.0005$ the jump at the composition interface near the point $x = 0.375$ occurs between the points $x = 0.34$ and $x = 0.408$, and the corresponding composition values are 0.00413818 and 0.987505, again within at least two digits of accuracy, which, again, is less than $h = 1/64$. The distance between the two points is $0.068 \approx 4.352h < 5h$; still less than the width of five cells with $h = 1/64$. Therefore, these two tests demonstrate that in the absence of other sources of error one can expect to resolve a compositional discontinuity to within less than five elements.

3.2. The computation of a falling box

In this section, we apply the DG-BP method to the sinking box problem first presented in Gerya and Yuen (2003a) in order to demonstrate the capabilities of a code designed around a characteristics-based, marker-in-cell method. Their problem is defined on a 2-D Cartesian domain that is 500 km × 500 km. A

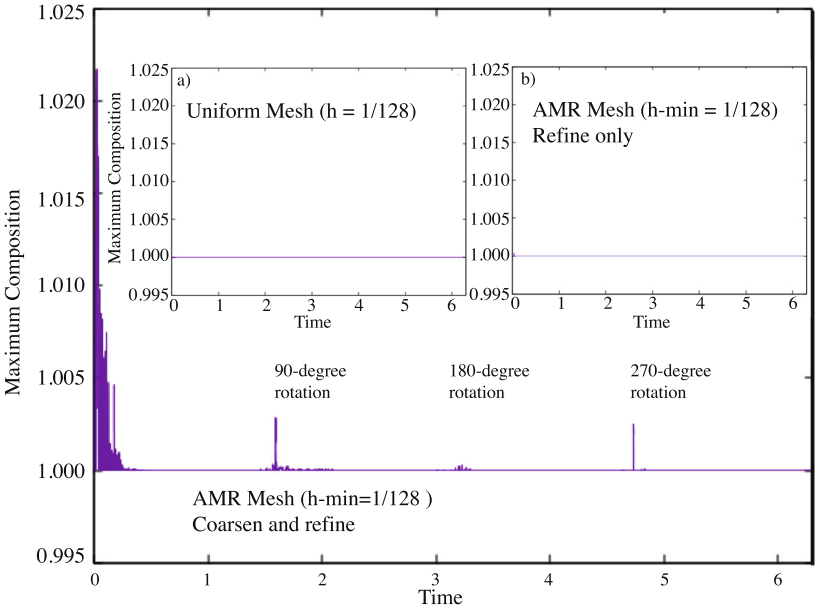

Fig. 3. 2D Circular Flow: the maximum composition with respect to time. The main figure is for an AMR mesh with coarsening and refinement of the mesh. Note the overshoot of the compositional field at the start of the computation and as the box shifts direction after every rotation of $\pi/2$. The errors occur because the AMR coarsening algorithm does not preserve the cell average of the composition. Inset (a) shows the same result, but for a uniform mesh – there is no overshoot. Inset (b) shows the same result, but for AMR allowing only refinement of the grid. A small overshoot occurs, but only for times from $t = 0.0355$ to 0.03725.

small block (100 km × 100 km) is placed with its top edge at 50 km below the top of the domain and centered horizontally (Fig. 4-a). The viscosity contrast between the box is varied as a way of testing the accuracy and stability of the numerical solution when there is a sharp contrast in material properties; specifically, density and viscosity.

We present numerical results for two of their examples. In both examples the following parameters are held fixed:

$$\begin{aligned} &\mathbf{g} = (0, 9.8)\ \mathrm{m/s^2}, && \text{acceleration due to gravity}\\ &\tilde{a} = 500\ \mathrm{km} && \text{domain height and width}\\ &\eta_0 = 10^{21}\ \mathrm{Pa\,s} && \text{background viscosity}\\ &\rho_0 = 3200\ \mathrm{kg/m^3}, && \text{background density}\\ &\rho_1 = 3300\ \mathrm{kg/m^3}, && \text{small box density} \end{aligned} \tag{24}$$

while the viscosity of the small box, η_1, is increased from 10^{21} Pa·s to 10^{22} Pa·s for each test; i.e., the viscosity contrast between the small block and the surrounding material is increased from 1 to 10. The initial location and dimension of the small box is defined using the composition field,

$$C_0(x,0) = \begin{cases} 1, & \text{if } (x,y) \in [\frac{3}{8}\tilde{a}, \frac{5}{8}\tilde{a}] \times [\frac{5}{8}\tilde{a}, \frac{7}{8}\tilde{a}] \\ 0, & \text{otherwise} \end{cases}. \tag{25}$$

In our work, we solve a dimensionless problem by rescaling the physical domain into a unit square and scaling the background viscosity and background density so as to have a constant value of 1. Using these values we have the following scaling for time

$$\tilde{t} = \frac{\eta_0}{\tilde{a}\,|g|\,\rho_0} = 6.377551 \times 10^{10}\,\mathrm{s} = 2.022308 \times 10^{-3}\,\mathrm{Myr}.$$

The mesh size and time step size referred to below are all based on the dimensionless problem values. Unless stated otherwise, in all of the following computations we use the same maximum refinement level $l = 10$. Therefore, the global minimum mesh size is $h = \sqrt{2}(\frac{1}{2})^{l-1} = \frac{\sqrt{2}}{512}$. In order to compare the numerical results at the same final time, the time-step size is determined by the numbers $\triangle t = \gamma 500h$ where $\gamma = 1$ or 1.5 for the viscosity ratio 1 or 10, respectively. We chose the fixed time-step size after experimenting with several different values of $\triangle t$.

In order to stabilize the numerical method, the DG method uses an upwind flux and the BP limiter, as well as the SSP time discretization scheme discussed in Section 2.1. For comparison we also run this falling box problem using FEM with the entropy-viscosity stabilization of the composition advection equation with an implicit-explicit BDF2 time discretization scheme. All tests are implemented using the deal.II C++ open source library (Bangerth

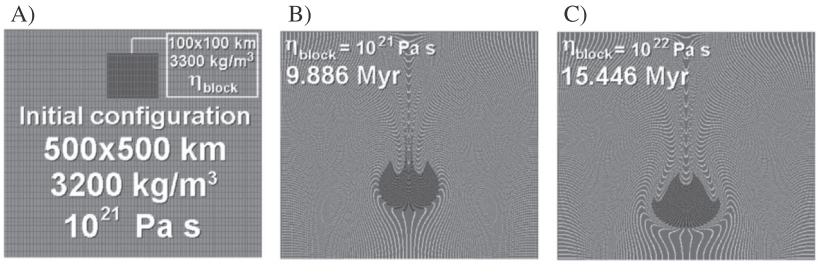

Fig. 4. Numerical results of the falling box from Gerya and Yuen (2003a). Black and white dots represent positions of markers for the block and the medium, respectively. Grid resolution of this model is 51 × 51 nodes, 22,500 markers. (A) Initial set-up, (B) Case $\eta_1/\eta_0 = 1$ after 9.886 Myr, (C) Case $\eta_1/\eta_0 = 10$ after 15.446 Myr. The initial set-up used in this study is identical to that shown in (A) except for a slightly different initial position and we use a compositional field instead of tracer particles.

et al., 2015). In these computations, we use the Taylor–Hood (or Hood-Taylor) elements for the numerical solution of the Stokes equations. Specifically, we use a second-order spatial element basis for the velocity field and a first-order spacial element basis for the pressure (in short, (Q_2, Q_1) elements for FEM velocity and pressure), a second order spatial element basis (i.e., a Q_2 element) for the FEM composition field, and a second order discontinuous spatial element basis (i.e., a Q_{-2} element) for the DG composition field.

The falling box problem is a good test case for our DG-BP method for several reasons. First, it is a simple model problem to implement. Second, it has a strong discontinuity in viscosity, which makes the numerical computation more challenging than for a constant viscosity ratio. (We have made computations up to a viscosity ratio of 10^6.) Third, the deformation of the box differs for different viscosity ratios, providing us with the opportunity to examine how the method performs for different shapes of compositional variation. For comparison, the numerical results for the same problem studied in Gerya and Yuen (2003a) are shown in Fig. 4. It is important to note that these figures only show the final positions of the tracer particles. In order to obtain a composition field such as the viscosity, one needs to perform a linear interpolation from the tracer particles onto the mesh. This sinking box problem has also been used to test other geodynamics codes (e.g., Thielulot (2011)).

3.3. Comparison of DG with and without a BP limiter

The DG and FVM methods have been shown to have better numerical stability and numerical convergence than the FEM method for problems that involve the advection of a conserved quantity. A first-order FVM such as the upwind method will maintain the upper and lower bounds of the analytic solution but is too diffusive to be effective in practice. However, in the absence of a limiter, the DG method will not satisfy the maximal principle or the bound preserving property.

In order to illustrate the importance of the BP limiter, we display the numerical results for the DG case using the second order SSP Runge–Kutta time discretization algorithm with and without a BP limiter in Fig. 5. For this test, we consider the viscosity variation to be constant; i.e., $\eta_1/\eta_0 = 1$. Thus, only the composition field and density have a discontinuity. For the AMR algorithm at time-step 2500 with $h = \frac{\sqrt{2}}{512}$ and time-step size $\triangle t = 1.38107$, the DG method needs more refinement near the discontinuous interface without applying the BP limiter (Fig. 5(A) left, # cells: 7465) than that with applying a BP limiter (Fig. 5(A) right, # cells: 6169). We zoom in on the compositional field in the top and bottom parts of the inner box in Fig. 5(B). The DG without the BP limiter results show a broad numerical boundary layer. Furthermore, the overshoot and undershoot without the BP limiter is over 24% and 16%, respectively. A horizontal profile (Fig. 5(C)) across the top part of the inner box confirms that the DG-BP method is much better at preserving a sharp compositional boundary. Therefore, for the remainder of the tests in this article, we always include the BP limiter to the DG method.

3.4. Comparison of the FEM and DG methods

To compare the numerical performance of the FEM with the DG method, we take two examples with the parameters given in (24) and the initial condition given in (25), but with each test using a different viscosity ratio; $\eta_1/\eta_0 = 1$ or 10.

3.4.1. Uniform grid

Since we use (Q_2, Q_1) Taylor–Hood elements for our numerical solution of the Stokes problem, the numerical velocity does not satisfy a point-wise divergence free condition. In order to study how such a non-divergence free velocity field can affect the performance of the DG-BP method, we first compute the problem with a unit viscosity ratio on a uniform grid with a mesh size of $h = \frac{1}{128}\sqrt{2}\tilde{a}$ km as shown in Fig. 6. Using a uniform mesh, the DG-BP results only show an overshoot of 0.001% and no undershoot to within an accuracy of $O(10^{-11})$. However, the FEM results show a significantly larger overshoot and undershoot of 0.087% and 0.249%, respectively.

Next, we measure the jump in the composition field along the vertical line $x = 0.415\tilde{a} = 207.5$ km at the final computational time $t = 8.089$ Myrs (Fig. 6; Table 3). For the DG-BP method, the width of the jump at the head (bottom) is less than 5 h, which is similar to that found in our point-wise divergence-free circular-flow computation above. However, the jump on the tail side is 3.5 times wider; this larger error is a result of not meeting the pointwise divergence free requirement. In the FEM computation the width in the composition jump is 25–38% wider than in the DG-BP computation of the same problem and has a much shallower slope over the full width as compared to the DG-BP profile (see Fig. 6). Furthermore it is apparent from the inset in Fig. 6 that in the FEM computation the jump at the tail is smeared over significantly larger region, with a consequent loss of the fine scale resolution of the jump itself. (See also Fig. 10 below.).

3.4.2. AMR grid

Calculations using AMR use fewer elements than uniform mesh calculations, therefore we next explore the effect of combining AMR with the DG-BP method for the falling box problem. As we can see from the figures of the composition field, the DG-BP method and FEM achieve similar accuracy and preserve the bound (between 0 and 1) within an accuracy of less than 0.1% (Fig. Figs. 7 and 8; Table 2). However, the DG-BP method uses fewer cells and

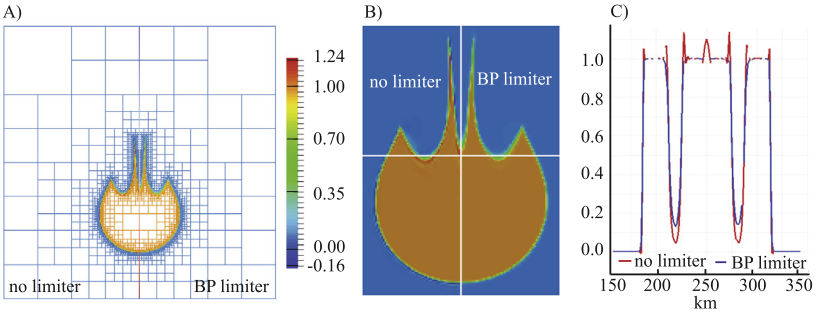

Fig. 5. Comparison of the DG method with and without the BP limiter. (A) Composition shown on and AMR grid at time-step 2500 (or $t = 6.982$ Myr) for DG without the limiter (left) and with the limiter (right), (B) An enlarged-view comparison of the compositional field of the falling box, (C) The horizontal profile across the top. The location of this profile is shown by the horizontal white line in (B).

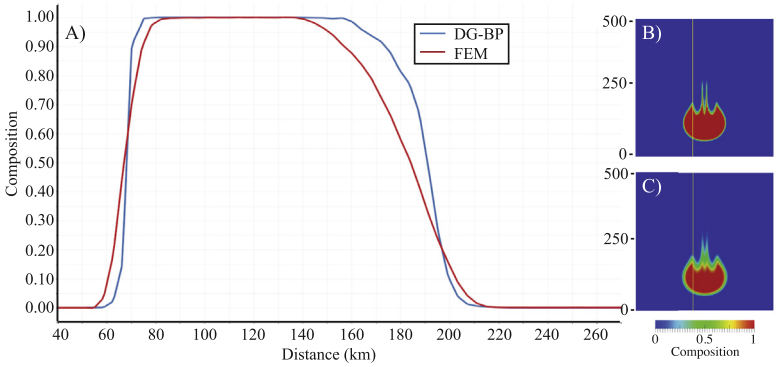

Fig. 6. Comparison of the compositional field for $\eta_1/\eta_0 = 1$. Composition shown for a uniform mesh with $h = \frac{1}{128}\sqrt{2}\bar{a}$ km and fixed time-step size $\triangle t = 2\bar{t}$, at time-step 2000 (i.e., $t = 4000\bar{t} = 8.089$ Myr). Vertical profiles are located at $x = 207.5$ km (see inset). Note that the computation made with the FEM is extremely diffusive. This is partly due to the use of an 'artificial diffusivity' to stabilize the advection algorithm.

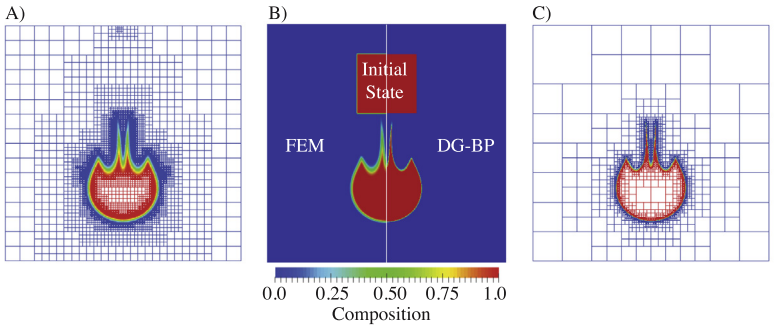

Fig. 7. Comparison of Compositional Field for Case $\eta_1/\eta_0 = 1$. Composition shown on AMR mesh at time $t = 6.982$ Myr, (A) FEM and (C) DG method with BP limiter. (B) Compositional field at initial time (top) and time $t = 6.982$ Myr (bottom) for FEM (left) and DG-BP (right).

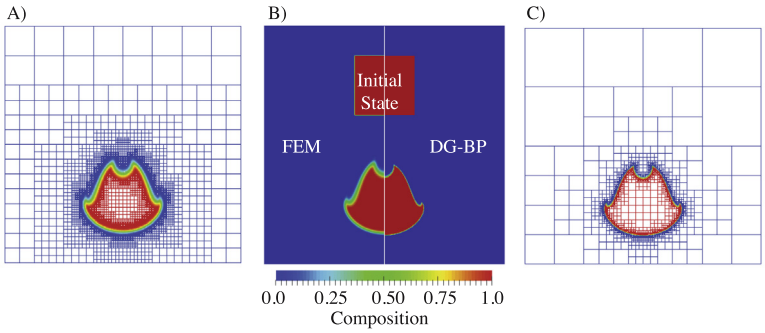

Fig. 8. Comparison of Compositional Field for Case $\eta_1/\eta_0 = 10$. Composition shown on AMR mesh at time $t = 10.474$ Myr for, (A) FEM and (C) DG method with BP limiter. (B) Compositional field at initial time (top) and time $t = 10.474$ Myr (bottom) for FEM (left) and DG-BP (right).

therefore, fewer degrees of freedom for the Stokes solver (see also Table 2).

We zoom in on the compositional field in the top part of the inner box in Fig. 9. The FEM results show a smooth, broad (smeared out) numerical boundary layer. The smoothing effect extends into the tails forming above the deformed corners of the box in the case with $\eta_1/\eta_0 = 1$ and has the effect of truncating the length of the full compositional anomaly and smearing the tails together (Fig. 10). The DG-BP method preserves much sharper boundaries between the tails and shows that the full compositional anomaly extends to the narrow tip of the tail.

Finally, the importance of using a second order SSP time discretization scheme is demonstrated by comparing to the results for the DG method using a first order forward Euler time discretization scheme (Fig. 10 C, F). The lower order time discretization scheme causes the boundary layer to smear out and causes oscillations within this smeared boundary layer. Therefore, the second order SSP Runge–Kutta time discretization scheme is necessary to preserve sharp, non-oscillatory compositional boundary when applying the DG method with the BP limiter.

4. Discussion

Our numerical results demonstrate the capabilities and limitations of the DG-BP method. For the circular flow problem, which is point-wise divergence free, on a uniform mesh there is no overshoot or undershoot to within the expected precision of the com-

Table 2
Comparison of Numerical Test Results for the Falling Box Problem: This data is at the final time $t = 6.982$ Myr, $t = 10.474$ Myr for viscosity ratio = 1, 10, respectively. For each viscosity ratio, we list the number cells in the AMR grid, the number of degrees of freedom for the Stokes system $(\mathbf{u}+p)$ and the advection solver (C), and the over-/undershoot error in the compositional field C as a percentage. Mesh size, h_{min}, is in units of $\sqrt{2}\bar{a}$ km. For the DG-BP with SSP RK2, the difference in the error for the uniform versus AMR grid represents the error due to the grid coarsening algorithm and the difference in minimum mesh size for these two cases.

η_1/η_0	Mesh	h_{min}	# Cells	# DOFs $(\mathbf{u}+p, C)$	Under C	Over C
FEM						
1	Uniform	1/128	16,384	(148,739, 66,049)	0.249%	0.087%
1	AMR	1/512	20,272	(189,353, 84,147)	0.094%	0.021%
10	AMR	1/512	16,840	(157,495, 69,989)	0.041%	0.028%
DG-BP with SSP and RK2						
1	Uniform	1/128	16,384	(148,739, 147,456)	0.000%	0.001%
1	AMR	1/512	6169	(63,020, 55,521)	0.013%	0.025%
10	AMR	1/512	4954	(50,910, 44,586)	0.000%	0.016%
DG-BP with 2nd order multi-step SSP						
1	AMR	1/512	6178	(63,110, 55,602)	0.016%	0.010%
10	AMR	1/512	4990	(51,153, 44,910)	0.010%	0.017%

Table 3
Width of the jump in the composition field for the Falling Box Problem for $\eta_1/\eta_0 = 1$. The values are measured along the vertical line from y_{min} to y_{max} at $x = 0.415\bar{a}$ km. 'Head' refers to the bottom of the falling box. 'Tail' refers to the upward-deflected corners at the upper edge of the box.

Method	Location	y_{min}	y_{max}	$C(y_{min})$	$C(y_{max})$	Width
FEM	Head	0.11	0.168	0.00141761	0.995297	7.424 h
DG-BP	Head	0.118	0.15	0.00326439	0.996589	4.096 h
FEM	Tail	0.278	0.432	0.996832	0.00450687	19.712 h
DG-BP	Tail	0.314	0.424	0.995551	0.0050364	14.08 h

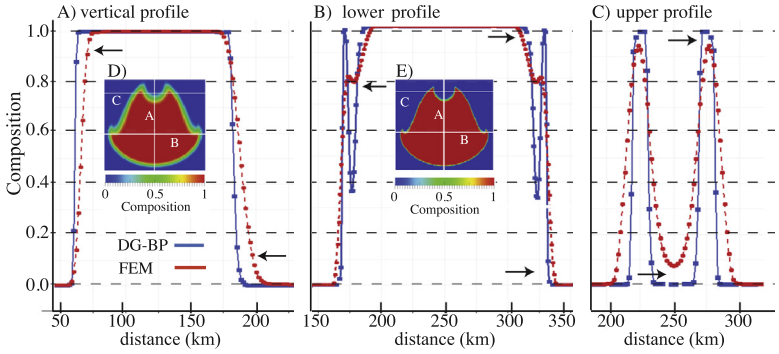

Fig. 9. Profiles of Compositional field across falling block for case with $\eta_1/\eta_0 = 10$. (A) Vertical profile bisecting falling block: DG – blue, FEM – red. (B) Horizontal profile across bottom edge. (C) Horizontal profile across top. Location of profiles are shown in (D) for DG result and (E) for FEM result. Arrows point to locations where the differences between the two results clearly illustrate the strengths (sharp compositional boundaries for DG method) and weaknesses (significant smoothing for FEM method) of each method. (For interpretation of the references to colour in this figure legend, the reader is referred to the web version of this article.)

putation. Furthermore, the jump in the composition field occurs over less than five elements independent of mesh size. When we use AMR the interpolation in the grid coarsening algorithm introduces an over-/undershoot error of about 2%; this error occurs because the cell average is not preserved during grid coarsening. When the DG-BP method is applied to a dynamic flow field that is not pointwise divergence free, the over/ undershoot error is about 0.001% on a uniform mesh (with $h = 1/128$), and increases to 0.013–0.025% using AMR (for $h = 1/512$). This source of error can be eliminated by choosing an element type that will give a point-wise divergence free solution for the Stokes equations (e.g., see Raviart and Thomas (1977)). Compared to the FEM solution with entropy-viscosity stabilization the over-/undershoot values are similar, but the DG-BP method uses fewer elements and fewer degrees of freedom. This is because the compositional jump is sharper, and therefore the AMR algorithm requires a smaller region for the fully refined grid.

Thus, some of the limitations of DG-BP method shown in the our article can be remedied because, as is common in mantle convection codes, we use Taylor–Hood elements. For this choice of element, the computed velocity is pointwise divergence free. This will introduce a small error that is $\mathcal{O}(h)$. Application of the BP limiter requires that the flow is point-wise divergence free in order to maintain the global bounds on the composition field; $C \in [0, 1]$. Because this requirement is violated by the choice of (Q_2, Q_1) elements, the BP limiter is unable to maintain a strict bound on the composition field. One example of an element that is pointwise divergence free is a Raviart–Thomas element (Raviart and Thomas, 1977). However, we note that using a different element type may require more degrees of freedom, and hence, one should first determine that the underlying goals of the research require more precise tracking of the compositional boundary. One might also consider other boundary tracking methods such as particles and true front tracking.

In addition, as we have shown in the derivation of the DG-BP method in Section 2.5, the cell average is an important factor in defining the BP-limiter. The current implementation of the AMR algorithm provided in the deal.II package does not preserve the cell

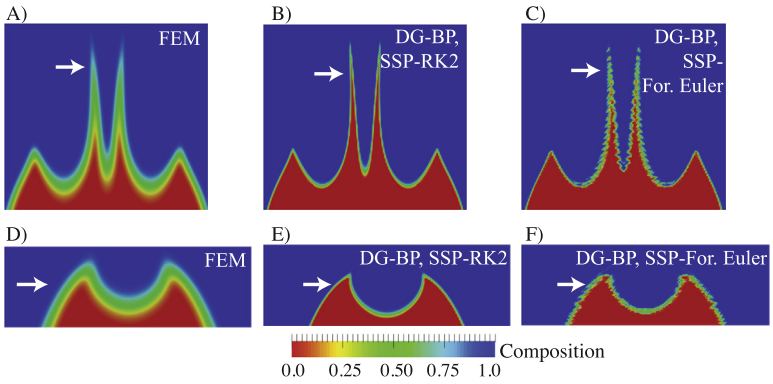

Fig. 10. Enlarged-view Comparison of Compositional Field for Top of Falling Box. Case with $\eta_1/\eta_0 = 1$ with (A) FEM, (B) DG with BP limiter and second order SSP RK2 time-step algorithm, and (C) DG with BP limiter and 1st order forward Euler algorithm. Case with $\eta_1/\eta_0 = 10$ with (D) FEM, (E) DG with BP limiter and second order SSP RK2 time-step algorithm, and (F) DG with BP limiter and 1st order forward Euler algorithm. Arrows point to tail (top) and corner (bottom) features discussed in the text.

average when the grid is coarsened. In addition, when the AMR algorithm is coupled with Taylor–Hood elements the error introduced by the element type is magnified. Modifying the AMR algorithm to preserve the cell average should remove this source of error.

4.1. Implications for geodynamics simulations

As discussed in the introduction, the choice of which method one uses to track a composition field within a mantle convection computation depends on many factors, foremost of which is the problem one wishes to address. Additional factors include the level of accuracy that is required, subject to the available computational resources and how the composition field(s) 'interacts' with other essential properties (e.g., density, viscosity) of the computed solution.

In order to illustrate these considerations for a specific problem we present some results for an isoviscous Rayleigh–Taylor problem in a two-dimensional rectangle, in which the buoyant fluid layer lies beneath a denser layer, with a perturbed interface between the two layers (van Keken et al., 1997). This problem, often referred to as the 'van Keken problem', has been a widely used by researchers in computational geodynamics (e.g., Kronbichler et al. (2012)).

In our computations we have used the same parameter file *van-keken-smooth.prm* for the 'van Keken thermochemical composition problem' provided with the open-source mantle convection code ASPECT (Bangerth and Heister, 2015). Note that in the initial conditions for this particular computation the discontinuous jump is replaced with a jump that is smoothed (Fig. 11(A)). We refer the interested reader to van-keken-smooth.prm for the precise formulation of the initial conditions. Also, please note that due to limitations in the current release of ASPECT, the DG-BP limiter has only been implemented in ASPECT with an implicit backward Euler time discretization algorithm, not the more effective SSP algorithm.

Fig. 11(A) shows the initial conditions. The final numerical results at time $t = 2000$ are shown in Figs. 11(B)–(C). In Fig. 11 (E)–(F) we compare the DG-BP and FEM profiles along the vertical line at $x = 0.45$ and the horizontal line at $y = 0.85$ with two uniform refinements of 128×128 and 256×256 cells). In addition, in Fig. 11(D) we have plotted the evolution of the Root Mean Square (RMS) velocity as a function of time for the two different of global mesh refinements for both the FEM and DG-BP computations.

Although the RMS-velocity for the FEM and DG-BP simulations are almost identical, the FEM results show more smearing of the interface boundaries. In addition, some features are missing in the FEM simulation in the less refined mesh, while other features are much broader than in the DG-BP simulation. Therefore, depending on the method one uses for this type of problem, one might draw different conclusions concerning the mixing process; e.g., the smallest scales of heterogeneity.

Similar considerations are important for the application of any compositional tracking method to problems of mantle mixing and entrainment (van Keken et al., 1997; Zhong and Hager, 2003; Leng and Zhong, 2011). In order to successfully address the entrainment problem with the DG-BP method presented here it would most likely be desirable to implement it with a point-wise divergence free element and with an improved AMR (coarsening) interpolation algorithm as discussed above.

While we have demonstrated some of the advantages of the DG-BP, the question remains for what types of problems might this be the preferred method for mantle convection computations. Here we address those questions that we consider essential for the kinds of models described in the introduction.

Advection–diffusion equation Our long-term goal is to extend the DG-BP method presented here to fields that satisfy advection–diffusion equation; in particular, the temperature coupled to the incompressible Stokes equations with a Boussinesq approximation for the density. The DG-BP method will be particularly important when one is interested in modeling problems in which the temperature has steep gradients, such as at the tip of a rapidly sinking slab in the upper mantle, and in which the viscosity depends exponentially on the temperature (Billen and Hirth, 2007; Burkett and Billen, 2009; Arredondo and Billen, 2016). For problems such as these, overshoots and undershoots in the temperature lead to unacceptable errors in the viscosity and a breakdown in the underlying accuracy and validity of the computation.

Our (preliminary) comparisons to the default algorithm for modeling the advection and diffusion of the temperature in ASPECT clearly show that the entropy-viscosity stabilization algorithm leads to a far too diffuse temperature field. Similar problems with the use of "artificial viscosity" in shock dynamics computations lead to the development of the plethora of slope limiting/bound preserving algorithms that are now considered state-of-the art in computational shock physics (Woodward and Colella, 1984). We note that for the same reasons Chi Wang Shu and his collaborators are now actively adopting these algorithms for use in FEM codes (Shu, 2016a; Shu, 2016b).

Tracking multiple compositional fields The DG-BP method presented in this article can also be used to track multiple compositional fields in the same model without any modifications to the algorithm. When there are multiple compositions and no reaction between them, one can still assume that each compositional field is bounded globally, since each composition satisfies the advection Eq. (1c) subject to (1b).

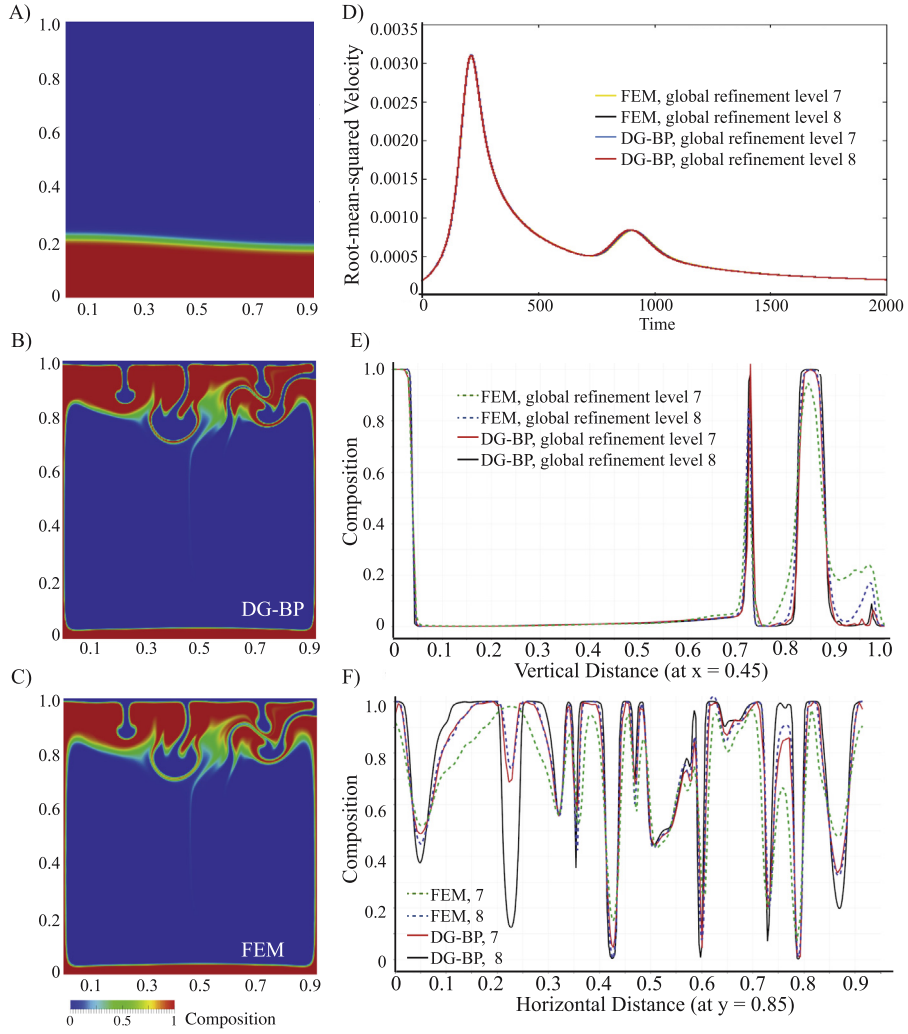

Fig. 11. (A) Initial composition on a uniform grid mesh with 256 × 256 cells. (B) DGBP result at final time $T = 2000$. (C) FEM result at final time $T = 2000$. (D) The composition profiles at vertical line $x = 0.45$. E) The composition profiles at horizontal line $y = 0.85$. (F) The Root Mean Square (RMS) velocity as a function of time for two different numbers of global mesh refinements for the FEM and DGBP.

Long-term stretching, mixing and folding Since the underlying DG discretization of the composition field allows for discontinuities at cell edges, as the composition field is stretched and breaks up into smaller pieces the boundaries between these fields will continue to be tracked and remain sharp. However, the accuracy of capturing the details of the mixing behavior is limited by the smallest mesh size, and therefore future work is needed to determine how the computational cost (as determined by the number of DOFs) increases as the composition is mixed at finer scales. The ability to maintain sharp boundaries through time in a computation is likely to influence conclusions related to the entrainment of compositional signals from boundary layers into rising thermal plumes. Our computational results indicate that coupling the method to AMR will limit the computational cost as mixing proceeds, at least until the mixing leads to compositional heterogeneity at all scales.

Use in both 2-D and 3-D simulations The DG-BP method can be used in both two and three dimensional computations without any modification.

4.2. Considerations for the optimal performance of the DG-BP method

Our numerical results clearly demonstrate several advantages when one uses the DG-BP method instead of a second-order accurate FEM advection algorithm with an entropy-viscosity stabilization technique. However, we have identified several requirements that must be met by the underlying FEM code – and the AMR algorithm if one is being used – in order to take full advantage of the DG-BP method as presented here. In short, in order for one to take full advantage of the DG-BP method it is necessary to use a pointwise divergence free element and an AMR algorithm that preserves the cell average during the coarsening and refinement step. (The AMR algorithm we used in this work preserved the cell average only when refining a cell/element.) Nevertheless, even without these additional features in the underly FEM code, the DG-BP method has over-/undershoot errors that are comparable to the FEM method with entropy-viscosity stabilization, but it does not smear the boundary or 'jump' between compositions as much as the entropy-viscosity method. Thus, when combined with an AMR algorithm the DG-BP method as presented here requires fewer degrees of freedom than an the FEM advection algorithm with a viscosity-entropy stabilization method. This is due to the much sharper representation of the steep gradients in the composition field (e.g., 'jumps') and hence the requirement for fewer refined cells in a neighborhood of these steep gradients/ jumps.

Finally, a theoretical consideration. The existence of a bound preserving limiter for any implicit time discretization scheme with

a DG method is still an open question. However, numerically one can attempt to use the bound preserving limiter with an implicit time discretization scheme and expect improved numerical results.

5. Conclusions

The advection of composition fields is an essential component of mantle convection computations; often requiring the tracking/-capturing of sharp boundaries between distinct compositions as they are subducted, mixed into the mantle, and entrained in upwellings. However, as discussed in the introduction, there are trade-offs one must make when using existing methods to model these problems; they can be computationally expensive, smear sharp boundaries, or are not easily adapted to computing the advection of multiple compositional fields. The computations presented in this article demonstrate that the DG method with a Bound preserving (BP) limiter is a stable, accurate and cost-effective approach for computing the advection of a non-diffusive compositional field in a velocity field given by the incompressible Stokes equations. In addition, this DG-BP method can be used to compute the advection of a multiple compositional fields through all the physical processes expected within the mantle (e.g., subduction, mixing, stretching, entrainment) in both two and three dimensions. In summary, it provides researchers in computational geodynamics with another useful option for modeling the advection of a compositional field in solid Earth geodynamics problems.

In future work we plan to study other methods for stabilizing the DG method for the composition advection equation with compressible flow, such as the weighted essentially non-oscillatory (WENO) scheme (Qiu and Shu, 2005; Zhu et al., 2008) and to apply the ideas that underlie the DG-BP method to advection–diffusion equations.

Acknowledgements

We would like to thank Shijie Zhong and an anonymous reviewer for thoughtful reviews that greatly improved the manuscript, Jon Robey for illuminating discussions concerning level set methods and high order time discretization approach, and John Naliboff for his helpful remarks concerning our manuscript. This work was supported by the National Science Foundation Grant No. 1440811.

References

Arredondo, K.M., Billen, M.I., 2016. The effects of phase transitions and compositional layering in two-dimensional kinematic models of subduction. J. Geodyn. 100, 159–174.
Bangerth, W., Heister, T., 2015. ASPECT: Advanced Solver for Problems in Earth's ConvecTion. Computational Infrastructure in Geodynamics.
Bangerth, W., Heister, T., Heltai, L., Kanschat, G., Kronbichler, M., Maier, M., Turcksin, B., 2015. The deal.II library, version 8.3. preprint.
Berger, M.J., Oliger, J., 1984. Adaptive mesh refinement for hyperbolic partial differential equations. J. Comput. Phys. 53 (3), 484–512.
Billen, M.I., Hirth, G., 2007. Rheologic controls on slab dynamics. Geochem. Geophys. Geosyst. 8.
Brooks, A.N., Hughes, T.J., 1982. Streamline Upwind/Petrov-Galerkin formulations for convection dominated flows with particular emphasis on the incompressible Navier-Stokes Equations. Comput. Methods Appl. Mech. Eng. 32, 199–259.
Burkett, E.R., Billen, M.I., 2009. Dynamics and implications of slab detachment due to ridge-trench collision. J. Geophys. Res. 114 (B12402).
Burstedde, C., Stadler, G., Alisic, L., Wilcox, L.C., Tan, E., Gurnis, M., Ghattas, O., 2013. Large-scale adaptive mantle convection simulation. Geophys. J. Int. 192 (3), 889–906.
Christensen, U., 1982. Phase boundaries in finite amplitude mantle convection. Geophys. J. R. Astron. Soc. 68, 487–497.
Christensen, U.R., 1989. Mixing by time-dependent convection. Earth Planet. Sci. Lett. 95, 382–394.
Christensen, U.R., 1996. The influence of trench migration on slab penetration into the lower mantle. Earth Planet. Sci. Lett. 140, 27–39.
Cockburn, B., Hou, S., Shu, C.-W., 1990. The Runge-Kutta local projection discontinuous Galerkin finite element method for conservation laws. IV. The multidimensional case. Math. Comput. 54 (190), 545–581.
Cockburn, B., Shu, C.-W., 1989. TVB Runge-Kutta local projection discontinuous Galerkin finite element method for conservation laws. II. General framework. Math. Comput. 52 (186), 411–435.
Cockburn, B., Shu, C.-W., 1998. The local discontinuous Galerkin method for time-dependent convection-diffusion systems. SIAM J. Numer. Anal. 35 (6), 2440–2463.
Cockburn, B., Shu, C.-W., 1998. The Runge-Kutta discontinuous Galerkin method for conservation laws V: Multidimensional systems. J. Comput. Phys. 141 (2), 199–224.
Davies, G.F., 1977. Whole-mantle convection and plate tectonics. Geophys. J. R. Astron. Soc. 49 (459–486).
Donea, J., Huerta, A., 2005. Steady transport problems, 33–78.
Farnetani, D.G., Richards, M.A., 1995. Thermal entrainment and melting in mantle plumes. Earth Planet. Sci. Lett. 136, 251–267.
Fischer, K.M., Ford, H.A., Abt, D.L., Rychert, C.A., 2010. The lithosphere-asthenosphere boundary. Ann. Rev. Earth Planet. Sci. 38, 551–575.
Garnero, E.J., McNamara, A.K., 2008. Structure and dynamics of Earth's lower mantle. Science 320, 626–628.
Gerya, T., 2010. Dynamical instability produces transform faults at mid-ocean ridges. Science 329 (1047).
Gerya, T.V., Yuen, D.A., 2003a. Characteristics-based marker-in-cell method with conservative finite-differences schemes for modeling geological flows with strongly variable transport properties. Phys. Earth Planet. Inter. 140, 293–318.
Gerya, T.V., Yuen, D.A., 2003b. Rayleigh-Taylor instabilities from hydration and melting propel 'cold plumes' at subduction zones. Earth Planet. Sci. Lett., 212
Gottlieb, S., 2005. On high order strong stability preserving Runge-Kutta and multi step time discretizations. J. Sci. Comput. 25 (1), 105–128.
Gottlieb, S., Shu, C.-W., Tadmor, E., 2001. Strong stability-preserving high-order time discretization methods. SIAM Rev. 43 (1), 89–112.
Guermond, J.-L., Pasquetti, R., Popov, B., 2011. Entropy viscosity method for nonlinear conservation laws. J. Comput. Phys. 230 (11). special issue High Order Methods for CFD Problems..
Gurnis, M., Hager, B.H., 1988. Controls of the structure of subducted slabs. Nature 335 (22), 317–321.
Hesthaven, J.S., Warburton, T., 2008. Nodal discontinuous Galerkin methods: algorithms, analysis, and applications. Springer.
Hoffman, N.R.A., McKenzie, D.P., 1985. The destruction of geochemical heterogeneities by differential fluid motions during mantle convection. Geophys. J. Int. 82 (2), 163–206.
Hofmann, A.W., 1997. Mantle geochemistry: the message from oceanic volcanism. Nature 385, 219–229.
Karason, H., van der Hilst, R.D., 2000. Improving global tomography models of P-wavespeed I. incorporation of differential travel times for refracted and diffracted core phases (PKP, Pdiff). J. Geophys. Res. 106, 6569–6587.
Kellogg, L.H., 1991. Interaction of plumes with compositional boundary at 670 km. Geophys. Res. Lett. 18 (5), 8650868.
Kellogg, L.H., Hager, B.H., van der Hilst, R.D., 1999. Compositional stratification in the deep mantle. Science 283, 1881–1884.
Kellogg, L.H., King, S.D., 1993. Effect of mantle plumes on the growth of D by reaction between the core and mantle. Geophys. Res. Lett. 29 (5), 379–382.
Kelly, D., Gago, D.S., Zienkiewicz, O., Babuska, I., et al., 1983. A posteriori error analysis and adaptive processes in the finite element method: Part I—error analysis. Int. J. Numer. Methods Eng. 19 (11), 1593–1619.
King, S.D., Raefsky, A., Hager, B.H., 1990. ConMan: vectorizing a finite element code for incompressible two-dimensional convection in the Earth's mantle. Phys. Earth Planet. Inter. 59, 195–207.
Kronbichler, M., Heister, T., Bangerth, W., 2012. High accuracy mantle convection simulation through modern numerical methods. Geophys. J. Int. 191 (1), 12–29. cited By 14.
Lenardic, A., Kaula, W.M., 1993. A numerical treatment of geodynamic viscous flow problems involving the advection of material interfaces. J. Geophys. Res. 98 (B5), 8243–8260.
Leng, W., Zhong, S., 2011. Implementation and application of adaptive mesh refinement for thermochemical mantle convection studies. Geochem. Geophys. Geosyst. 12 (4). http://dx.doi.org/10.1029/2010GC003425. n/a–n/a, q04006.
Lin, S.-C., van Keken, P.E., 2005. Multiple volcanic episodes of flood basalts caused by thermochemical mantle plumes. Nature 436, 250–252.
McNamara, A.K., Zhong, S., 2004. Thermochemical structures within a spherical mantle: superplumes or piles? J. Geophys. Res. 109 (B07402).
McNamara, A.K., Zhong, S., 2005. Thermochemical structures beneath Africa and the Pacific Ocean. Nature 437, 1136–1139.
Moresi, L.N., Dufour, F., Mulhaus, H.-B., 2003. A Lagrangian integration point finite element method for large deformation modeling of viscoelastic geomaterials. J. Comput. Phys. 184, 476–497.
Moresi, L.-N., Lenardic, A., 1997. Three-dimensional numerical simulations of crustal deformation and subcontinental mantle convection. Earth Planet. Sci. Lett. 150, 233–243.
Moresi, L.N., Solomatov, V.S., 1995. Numerical investigations of two-dimensional convection with extremely large viscosity variations. Phys. Fluids 9, 2142–2162.
O'Neill, C., Moresi, L., Müller, D., Albert, R., Dufour, F., 2006. Ellipsis 3D: a particle-in-cell finite-element hybrid code for modelling mantle convection and lithospheric deformation. Comput. Geosci. 32 (10), 1769–1779.

Oxburgh, E.R., Parmentier, E.M., 1977. Compositional and density stratification in oceanic lithosphere–causes and consequences. J. Geol. Soc. London 133, 343–355.
Qiu, J., Shu, C.-W., 2005. Runge–Kutta discontinuous galerkin method using weno limiters. SIAM J. Sci. Comput. 26 (3), 907–929.
Raviart, P.A., Thomas, J.M., 1977. A mixed finite element method for second order elliptic problems. In: Galligani, I., Magenes, E. (Eds.), Mathematical Aspects of Finite Element Methods: Proceedings of the Conference Held in Rome, December 10–12, 1975. Springer, Berlin Heidelberg, Berlin, Heidelberg, pp. 292–315.
Reed, W., Hill, T., 1973. Triangular mesh methods for the neutron transport equation.
Samuel, H., Evonuk, M., 2010. Modeling advection in geophysical flows with particle level sets. Geochem. Geophys. Geosyst. 11 (8), Q08020.
Shu, C.-W., 2016a. Discontinuous galerkin methods for time-dependent convection dominated problems: basics, recent developments and comparison with other methods. In: Building Bridges: Connections and Challenges in Modern Approaches to Numerical Partial Differential Equations. Springer, pp. 369–397.
Shu, C.-W., 2016b. High order weno and dg methods for time-dependent convection-dominated pdes. J. Comput. Phys. 316 (C), 598–613. http://dx.doi.org/10.1016/j.jcp.2016.04.030.
Suckale, J., Nave, J.-C., Hager, B.H., 2010. It takes three to tango: 1. Simulating buoyancy-driven flow in the presence of large viscosity contrasts. J. Geophys. Res. 115 (B07409).
Tackley, P.J., 2000. Mantle convection and plate tectonics: toward an integrated physical and chemical theory. Science 288, 2002–2007.
Tackley, P.J., 2012. Dynamics and evolution of the deep mantle resulting from thermal, chemical, phase and melting effects. Earth Sci. Rev. 110, 1–25.
Tackley, P.J., King, S.D., 2003. Testing the tracer ratio method for modeling active compositional fields in mantle convection simulations. Geochem. Geophys. Geosyst. (G^3) 4 (4), 8302.
Taylor, C., Hood, P., 1973. A numerical solution of the navier-stokes equations using the finite element technique. Comput. Fluids 1 (1), 73–100.
Thielulot, C., 2011. FANTOM: two and three-dimensional numerical modelling of creeping flows for the solution of geological problems. Phys. Earth Planet. Inter. 188, 47–68.
van Keken, P.E., King, S.D., Schmeling, H., Christensen, U.R., Neumeister, D., Doin, M.-P., 1997. A comparison of methods for the modeling of thermochemical convection. J. Geophys. Res. 102 (B10), 22477–22495.
Verfürth, R., 1996. A Review of a Posteriori Error Estimation and Adaptive Mesh-Refinement Techniques. John Wiley & Sons Inc.
Vynnytska, L., Rognes, M., Clark, S., 2013. Benchmarking FEniCS for mantle convection simulations. Comput. Geosci. 50, 95–105. benchmark problems, datasets and methodologies for the computational geosciences. http://www.sciencedirect.com/science/article/pii/S0098300412001689.
Woidt, W.-D., 1978. Finite element calculations applied to slat dome analysis. Tectonophysics 50, 369–386.
Woodward, P., Colella, P., 1984. The numerical simulation of two-dimensional fluid flow with strong shocks. J. Comput. Phys. 54, 115–173.
Zhang, X., Shu, C.-W., 2010a. On maximum-principle-satisfying high order schemes for scalar conservation laws. J. Comput. Phys. 229 (9), 3091–3120. http://www.sciencedirect.com/science/article/pii/S0021999109007165.
Zhang, X., Shu, C.-W., 2010b. On positivity-preserving high order discontinuous Galerkin schemes for compressible Euler equations on rectangular meshes. J. Comput. Phys. 229 (23), 8918–8934.
Zhang, Y., Zhang, X., Shu, C.-W., 2013. Maximum-principle-satisfying second order discontinuous Galerkin schemes for convection-diffusion equations on triangular meshes. J. Comput. Phys. 234, 295–316.
Zhao, C., Garnero, E.J., McNamara, A.K., Schmerr, N., Carlson, R.W., 2015. Seismic evidence for a chemically distinct thermochemical reservoir in Earth's deep mantle beneath Hawaii. Earth Planet. Sci. Lett. 426, 143–153.
Zhong, S., Hager, B.H., 2003. Entrainment of a dense layer by thermal plumes. Geophys. J. Int. 154 (3), 666–676. http://dx.doi.org/10.1046/j.1365-246X.2003.01988.x.
Zhong, S., Zuber, M.T., Moresi, L., Gurnis, M., 2000. Role of temperature-dependent viscosity and surface plates in spherical shell models of mantle convection. J. Geophys. Res. 105, 11063–11082.
Zhong, S.J., Yuen, D.A., Moresi, L.N., 2007. Numerical methods for mantle convection. In: Treatise on Geophysics. Elsevier, pp. 227–252. Ch. 7.05.
Zhu, J., Qiu, J., Shu, C.-W., Dumbser, M., 2008. Runge–Kutta discontinuous galerkin method using weno limiters II: unstructured meshes. J. Comput. Phys. 227 (9), 4330–4353.